



Constructing bimetal-complex based hydrogen-bonded framework for highly efficient electrocatalytic water splitting

Feng Qing Liu^{a,1}, Jian Wen Liu^{b,c,1}, Zhi Gao^{a,*}, Li Wang^a, Xian-Zhu Fu^{b,*}, Li Xiao Yang^a, Yuan Tao^a, Wen Hui Yin^a, Feng Luo^{a,*}

^a State Key Laboratory of Nuclear Resources and Environment, School of Chemistry, Biology and Materials Science, East China University of Technology, Nanchang, 330013, China

^b College of Materials Science and Engineering, Shenzhen University, Shenzhen, 518055, China

^c National Supercomputing Center in Shenzhen, Shenzhen, 518055, China

ARTICLE INFO

Keywords:

HOFs
Bimetal-complex
Bimetal effect
Water splitting
Synergic effect

ABSTRACT

We present herein a new concept of hydrogen-bonded organic framework (HOF) material for highly effective electrocatalysis of overall water splitting. This HOF material, namely HOF-Co, was synthesized based on very cheap raw materials. Crystallizing bimetallic HOFs of HOF-Co_xFe_{1-x} on nickel foam (NF) can be also easily obtained via a step-by-step approach. In 1 M KOH, HOF-Co_{0.5}Fe_{0.5} on the NF enables both excellent oxygen evolution reaction (OER) and hydrogen evolution reaction (HER) performance, thus leading to highly effective electrocatalysis of water splitting with a cell voltage of just 1.63 V at 10 mA cm⁻². The value is comparable to the commercial Pt/C/IrO₂ (1.59 V) and other established outstanding electrocatalysts. The mechanism, as evidenced by Density Functional Theory (DFT) calculations, is due to a significant synergistic effect from the abundant hydrogen-bond structure between coordinated water molecules and SO₄²⁻ ions that affords rich and accessible active sites, in conjunction with the bimetallic effect.

1. Introduction

Following the increasing energy demand and fast consumption of fossil fuels, it is urgent to develop new replaceable clean energy such as hydrogen energy [1–3]. Generally speaking, the hydrogen energy can be obtained by electrochemical water splitting through two half-reactions of HER and OER [4,5]. If without any assistance from catalyst, such water splitting process is high energy-consumption, thus, urgently requiring high-performance and stable electrocatalyst. Although commercial Pt/C and IrO₂ electrocatalysts can solve this issue, their abundance in nature is too low to meet the practical industry requirement [6–10]. Accordingly, searching for low-cost electrocatalysts, especially transition metal electrocatalysts with high abundance, is highly desirable [11–31].

Hydrogen-bonded organic frameworks (HOFs) presenting a new developed material platform are now receiving increasing attentions [32–43]. In principle, this class of material is constructed by supramolecular interactions such as hydrogen bonds, π - π stacking, and van der Waals interactions. This intrinsic character seriously restricts the stability of HOFs. And thereby in the literature only a few robust HOFs

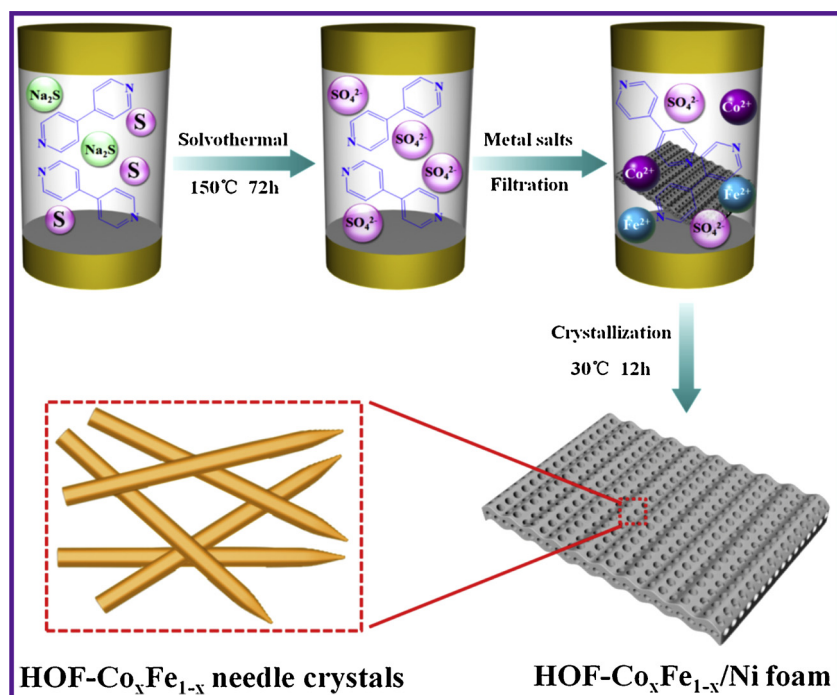
have been synthesized until now. Previous researches have disclosed their promising potential in gas storage, separation, and catalysis [44–48]. However, it should be pointed out that, to the best of our knowledge, until now there is still no report about utilizing HOF materials as electrocatalysts for water splitting, mainly due to its weak stability in strong alkaline environment usually employed for water splitting and extremely low activity [4,5]. Generally speaking, metal center such as Pt, Ir, and transition-metal of Co, Ni, Fe is viewed to provide high electrocatalytic activity for water splitting. Thereby, if continuing to follow the common molecular design rule, viz. the usage of pure organic linkers, to construct HOFs, undoubtedly we could not obtain suitable HOF electrocatalysts for water splitting. By contrast, given that we use metal-complex as building block to construct HOFs [43], then achievement of stable HOFs for electrocatalytic water splitting is expected. Moreover, the intrinsic nature of HOFs derived from supramolecular interactions is also believed to offer numerous active sites.

In this work, as shown in Scheme 1, we present the first case of using metal-complex based HOF for electrocatalytic water splitting. The HOF, HOF-Co, was prepared by a step-by-step approach by using very

* Corresponding authors.

E-mail addresses: gaozhi910201@163.com (Z. Gao), xz.fu@szu.edu.cn (X.-Z. Fu), ecitluofeng@163.com (F. Luo).

¹ These authors contributed equally to this work.



Scheme 1. A proposed draft of the step-by-step approach for *in situ* growing bimetal-complex based HOF materials on Ni foam, aiming at electrocatalysis of the overall water splitting.

cheap material source of S, Na₂S, 4,4'-bpy (4,4'-bipyridine), and metal salt source. Most importantly, such step-by-step approach facilitates to modulate the electronic structure of metal center by bimetallic method and *in-situ* grow HOF crystal on the nickel foam support. As a result, outstanding electrocatalytic performance of reaching 10 mA cm⁻² current density just with a low cell voltage of 1.63 V for water splitting is observed for the material of bimetal **HOF-Co_{0.5}Fe_{0.5}** *in situ* grown on Ni foam.

2. Experimental

2.1. Materials and characterizations

All reagents were commercially available and were directly used without further purification. Single crystal X-ray diffraction was carried out on a Bruker Smartbreeze instrument. Power X-ray diffraction (PXRD) of as-prepared samples were determined on a Bruker AXSD8 Discover powder diffractometer at 40 kV, 40 mA for Cu K α , ($\lambda = 1.5406 \text{ \AA}$). X-ray photoelectron spectra (XPS) measurements were performed in a Theta probe (Thermo Fisher) using monochromated Al K α radiation at $h\nu = 1486.6 \text{ eV}$. The scanning electron microscopy (SEM) images were obtained on a Oxford X-max microscope. The Transmission electron microscopy (TEM) and High-resolution TEM (HRTEM) were performed using a JEM-2010 transmission electron microscope operating at 200 kV. Thermogravimetric analysis (TGA) was performed using a TGA Q500 thermal analysis system under N₂ atmosphere. Elemental analysis of metal in samples was performed using a Shimadzu ICPS-7500 inductively coupled plasma emission spectrometer (ICP-AES).

2.2. Synthesis of HOF-Co_{1-x}Fe_x

Firstly, 4,4'-bipyridine (2.23 mmol, 0.3648 g), Na₂S (2.53 mmol, 0.1973 g), and S (2.53 mmol, 0.081 g) were dissolved in 16.7 mL of deionized water to form a mixed solution. Then, the solution was transferred into an autoclave (20 mL) with a Teflon liner, followed by hydrothermal treatment at 150 °C for 72 h with a ramp rate of 1 °C/min

and then cooled down to 70 °C at a ramp rate of 0.1 °C/min. The as-obtained pink solution was transferred to sealed glass bottle and the total amounts of 2.25 mmol for Co(NO₃)₂·6H₂O and FeSO₄·7H₂O with the Fe/Co molar ratio of 0/1, 0.8/0.2, 0.5/0.5, 0.2/0.8, 1/0 were subsequently added, respectively, followed by filtration. The obtained clear solution was crystallized at 30 °C for 12 h to obtain needle crystals. The HOF-Co_{1-x}Fe_x with different Co contents ($x = 0, 0.2, 0.5, 0.8, 1.0$) was denoted as HOF-Co, HOF-Co_{0.8}Fe_{0.2}, HOF-Co_{0.5}Fe_{0.5}, HOF-Co_{0.2}Fe_{0.8}, HOF-Fe, respectively.

2.3. In situ growing HOF crystal on Ni foam

This synthesis is similar to that as employed for preparation of HOF crystal, except for adding Ni foam (1.0 cm × 2.0 cm) to the filtrated solution after the introduction of metal ions. The obtained NF-supported materials are dried under atmosphere and then used to test electrochemical performance. The amount of HOFs grown on Ni foam determined by the weight difference of Ni foam before and after material grown is approximately 2 mg cm⁻².

2.4. X-ray crystallography

X-ray diffraction data of HOF-Co and HOF-Fe were collected at room temperature on a Bruker-AXS SMART Breeze CCD diffractometer using graphite monochromated Mo K α radiation ($\lambda = 0.71073 \text{ \AA}$). The data reduction included a correction for Lorentz and polarization effects, with an applied multi-scan absorption correction (SADABS). The crystal structure was solved and refined using the SHELXTL program suite. Direct methods yielded all non-hydrogen atoms, which were refined with anisotropic thermal parameters. All hydrogen atom positions, except for that on water molecules which are found first, were calculated geometrically and next were riding on their respective atoms. CCDC 1890647–1890648 contains the supplementary crystallographic data of HOF-Co and HOF-Fe, respectively. These data can be obtained free of charge from the Cambridge Crystallographic Data Centre via www.ccdc.cam.ac.uk/data_request/cif.

2.5. Electrochemical measurements

The catalyst inks were prepared by dispersing 5 mg catalyst into 1 mL solution composed of 0.95 mL isopropanol and 0.05 mL 0.5 wt% Nafion solution, followed by ultrasonication for 30 min to form a homogeneous ink. Then, 30 μ L of above ink was dropped on GC electrode and dried completely at room temperature. A glassy carbon (GC) disk electrode (5 mm in diameter) was used as the working electrode, while similar HOFs/Ni foam (1.0 cm \times 2.0 cm) prepared by dropping method or in-situ growth manner was directly used as the working electrode. When the HOFs/Ni foam was used as the working electrode, the area of submerged part of electrolyte is 1.0 cm² (1.0 cm \times 1.0 cm). All electrochemical measurements were performed in a standard three-electrode system by a CHI660E electrochemical workstation at room temperature.

For OER, a saturated calomel electrode (SCE) as reference electrode, a Pt electrode as the counter electrode, and the GC electrode with dropped HOF material (or NF electrode with dropped HOF material, or NF electrode with in-situ grown HOF crystal) as the working electrode was used. For HER, a saturated calomel electrode (SCE) as reference electrode, a carbon rod electrode as the counter electrode, and NF electrode with in-situ grown HOF crystal as the working electrode was used. For the overall water splitting, a two-electrode system based on HOF-Co_{0.5}Fe_{0.5}/NF electrode was used.

Linear sweep voltammetry (LSV) and chronoamperometry with a scan rate of 5.0 mV s⁻¹ were conducted in O₂-saturated 1.0 M KOH. The cyclic voltammogram (CV) was performed at a scan rate of 100 mV s⁻¹ for 1000 cycles and the chronoamperometric curves were recorded at the overpotential of 278 mV for OER and 170 mV for HER to determine the stability of Co_{0.5}Fe_{0.5}-EUCT. The electrochemically active surface area (ECSA) of different catalysts was determined based on the double-layer capacitance (*C_{dl}*) using a simple cyclic voltammetry method. Electrochemical impedance spectroscopy (EIS) measurements were carried out by applying an AC voltage with 5 mV amplitude over a frequency range from 100 kHz to 0.1 Hz at the overpotentials of 278 mV for OER and 170 mV for HER. All the potentials were referenced to a reversible hydrogen electrode (RHE) without *iR*-compensation.

Turnover frequency (TOF) values of different electrodes were calculated based on the equation: TOF = (*J* \times *A*) / (4 \times *F* \times *n*), where *J* (mA/cm²) is the current density at the overpotential of 400 mV for OER and 200 mV for HER; *A* is the surface area of electrode (1 cm²); *F* is the Faraday constant (96,485 C/mol); *n* is molar number of active sites on the electrode. In this work, both Co and Fe in HOFs samples are regarded as active sites.

2.6. Computational details

The spin-polarized DFT calculations were performed using the Vienna Ab-initio Simulation Package [49]. The generalized gradient approximation (GGA) with the Perdew-Burke-Ernzerhof (PBE) functional was used to describe the electronic exchange and correlation effects [50]. One unit cell of the HOF-Co with the obtained parameters experimentally *a* = *b* = 11.4062 Å, *c* = 20.8612 Å, α = β = 90°, γ = 120° to model the HOF-Co theoretically. In addition, 1, 3, 5 and 6 Co atoms were substituted by Fe atoms to model the HOF-Co_{0.83}Fe_{0.17}, HOF-Co_{0.50}Fe_{0.50}, HOF-Co_{0.17}Fe_{0.83} and HOF-Fe, respectively. The gamma point was used for geometric optimization with a cutoff energy of 500 eV. The criteria for the geometry optimization and ionic steps were set as 0.02 eV/Å and 10⁻⁶ eV for the force and energy, respectively. The DFT-D3 method of Grimme was used to take into account the dispersive interactions.

Following Nørskov's strategy [51], the adsorption energies (ΔE) of intermediates (OH, O, OOH and O₂) on substrate were described as:

$$\Delta E(\text{OH}) = E(\text{sub}/\text{OH}) - [E(\text{sub}) + E(\text{H}_2\text{O}) - E(\text{H}_2)/2]$$

$$\Delta E(\text{O}) = E(\text{sub}/\text{O}) - [E(\text{sub}) + E(\text{H}_2\text{O}) - E(\text{H}_2)]$$

$$\Delta E(\text{OOH}) = E(\text{sub}/\text{OOH}) - [E(\text{sub}) + 2^*E(\text{H}_2\text{O}) - 3^*E(\text{H}_2)/2]$$

$$\Delta E(\text{O}_2) = E(\text{sub}/\text{O}_2) - [E(\text{sub}) + 2^*E(\text{H}_2\text{O}) - 2^*E(\text{H}_2)]$$

Where $\Delta E(\text{OH})$, $\Delta E(\text{O})$, $\Delta E(\text{OOH})$ and $E(\text{sub}/\text{O}_2)$ are the total energies of O, OH, OOH and O₂ groups on the substrate, respectively; $\Delta E(\text{sub})$, $E(\text{H}_2\text{O})$, and $E(\text{H}_2)$ denote the total energies of bare substrate, water, and hydrogen gas, respectively.

To account for the contribution from entropy, temperature and zero point energy, the Gibbs free energies of the intermediates was calculated at 298.15 K, and the Gibbs free energy change (ΔG) for the adsorption of intermediates H, OH, O, OOH and O₂ was calculated by

$$\Delta G = \Delta E + \Delta \text{ZPE} - T\Delta S$$

Where the *E*, *ZPE*, *T*, and *S* denote the calculated total energy, zero point energy, temperature, and entropy.

3. Results and discussion

These metal-complex based HOFs were prepared through a step-by-step approach, as shown in Scheme 1. Firstly, the hydrothermal synthesis of S, Na₂S and 4,4'-bpy was performed to *in situ* generate mixed ligands of SO₄²⁻ and 4,4'-bpy by oxidation reaction at 150 °C for 72 h with a ramp rate of 1 °C/min. After cooling the temperature to 70 °C, monometal or bimetal ions were added into the above mixed ligand solution of SO₄²⁻ and 4,4'-bpy. After carefully controlling the solvothermal temperature, the monometal- or bimetal-complex based HOF crystals were successfully obtained. For comparison, S and Na₂S were replaced by Na₂SO₄ ligand, and then the same synthesis procedures were carried out. It was found that the HOF crystals can not be obtained, which indicates that the oxidation process of S and Na₂S to SO₄²⁻ can provide unique environment for the growth of HOF crystals. The *in situ* growth of HOF crystals on NF (HOF/NF) was executed by immersing activated NF on the above obtained ligand solution of SO₄²⁻ and 4,4'-bpy, along with the addition of monometal or bimetal ions. The activated NF can provide rough surface, which should be good for the nucleation and growth of HOFs crystals. Co and Fe all belong to the transition metal and the crystal structure of HOF-Co and HOF-Fe is determined by single crystal X-ray diffraction, indicative of *P6₁* or *P6₅* space group and isomorphous structure of them. Isomorphous structure of HOF-Co_{0.8}Fe_{0.2}, HOF-Co_{0.5}Fe_{0.5}, and HOF-Co_{0.2}Fe_{0.8} was confirmed by tracing their cell parameters. Thus, only the representative complex of HOF-Co is discussed in more detail. The Co site takes the common octahedral geometry finished by three terminally coordinated water molecules, two 4,4'-bpy nitrogen atoms, and one SO₄²⁻ oxygen atom (Fig. 1a). Due to SO₄²⁻ just playing terminal coordination role, Co(II) ions along *b* axis are bridged by 4,4'-bpy ligands to construct a 1D metal complex (Fig. 1b). Interestingly, abundant hydrogen bonds between SO₄²⁻ and coordinated water molecules with the bond distance of 2.72 Å and bond angle of 140.64° are observed among this 1D metal complex, resulting in the overall 3D supramolecular metal-complex based HOF framework (Fig. 1c). Further check the HOF framework disclose that if without the consideration of metal ions and 4,4'-bpy ligand, hydrogen-bonded nanotube just composed of SO₄²⁻ and coordinated water molecules is observed. And further through sharing SO₄²⁻ and hydrogen bond interactions an overall 3D hydrogen-bonded nanotube-based framework just built on SO₄²⁻ and coordinated water molecules is generated (Fig. 1d).

To further characterize these HOFs, scanning electron microscopy (SEM), X-ray photoelectron spectra (XPS), Energy-dispersive X-ray spectroscopy (EDS), thermogravimetric analysis (TGA), power X-ray diffraction (PXRD) and inductively coupled plasma atomic emission spectroscopy (ICP-AES) analysis are employed. SEM images demonstrate that these HOFs are uniform rod-like crystals (Fig. 2a and S1). As evidenced by XPS and EDS mapping, the HOF-Co_{0.5}Fe_{0.5} is composed of

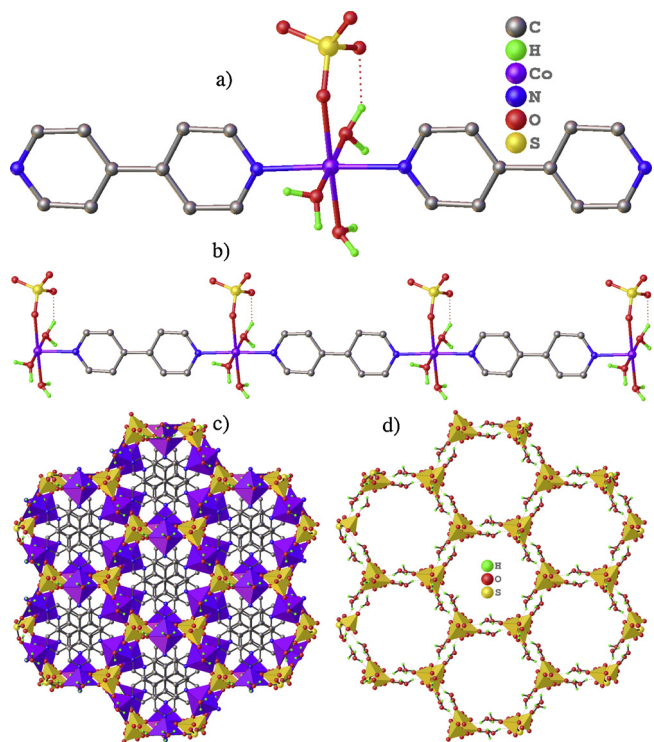


Fig. 1. View of the structure of HOF-Co. a) The coordination surrounding of metal ion. b) The 1D metal complex connected by 4,4'-bpy ligand and contains abundant coordinated water molecules. c) The 3D framework of HOF-Co. Metal and SO_4^{2-} ions give the octahedral and tetrahedral configuration, respectively. d) The 3D hydrogen-bonded nanotube-based framework just built on SO_4^{2-} and coordinated water molecules.

C, O, N, S, Co and Fe (Fig. 2b, S2, and S3) and the uniform distribution of these elements within HOFs was observed. The EDS mapping images of other HOFs are shown in Fig. S4. Transmission electron microscopy (TEM) and High-resolution TEM (HRTEM) images further determine the rod-like morphology of HOF- $\text{Co}_{0.5}\text{Fe}_{0.5}$ crystal (Fig. S5). TGA indicates the release of both free and coordinated water molecules before 160°C (Fig. S6). The PXRD patterns of these HOFs exhibit similar diffraction peaks, which match well with the simulated pattern obtained from single crystal data (Fig. 2c), indicative of their good crystallinity, high phase purity, and isomorphous structure. The molar ratios of Co/Fe in these bimetallic HOFs were determined by inductively coupled plasma atomic emission spectroscopy (ICP-AES) (Table S1).

The electrocatalytic performance of these HOFs was initially investigated toward OER in 1.0 M KOH by dropping on glassy carbon electrode (GC) with a loading of about 0.340 mg cm^{-2} . All the data were obtained without IR-correction. As shown in Fig. 2d, bimetal HOFs show much better activity than monometallic HOFs (HOF-Co and HOF-Fe). Among different bimetallic HOFs, HOF- $\text{Co}_{0.5}\text{Fe}_{0.5}$ exhibits the lowest overpotential of 364 mV at the current density of 10 mA cm^{-2} and a hierarchy of HOF- $\text{Co}_{0.5}\text{Fe}_{0.5}$ (364 mV) > HOF- $\text{Co}_{0.2}\text{Fe}_{0.8}$ (381 mV) > HOF- $\text{Co}_{0.8}\text{Fe}_{0.2}$ (397 mV) > HOF-Fe (413 mV) > HOF-Co (459 mV) is observed, strongly suggesting a bimetallic synergetic effect on OER performance. Notably, the corresponding Tafel slope and charge transfer resistance of HOF- $\text{Co}_{0.5}\text{Fe}_{0.5}$ are also the smallest and show the same hierarchy (as observed in overpotential) with other HOFs (Fig. S7), implying that such material also affords more fast OER rate and charge transfer kinetics. The electrochemically active surface area (ECSA) determined by the double-layer capacitance using cyclic voltammogram (CV) method reveals that HOF- $\text{Co}_{0.5}\text{Fe}_{0.5}$ has the largest ECSA (4.15 mF cm^{-2}), which is about 2.5, 4.2, 9.2, 13.8 times higher than that of HOF- $\text{Co}_{0.2}\text{Fe}_{0.8}$, HOF- $\text{Co}_{0.8}\text{Fe}_{0.2}$, HOF-Fe and HOF-Co, respectively (Fig. S8), highlighting the high activity of HOF- $\text{Co}_{0.5}\text{Fe}_{0.5}$.

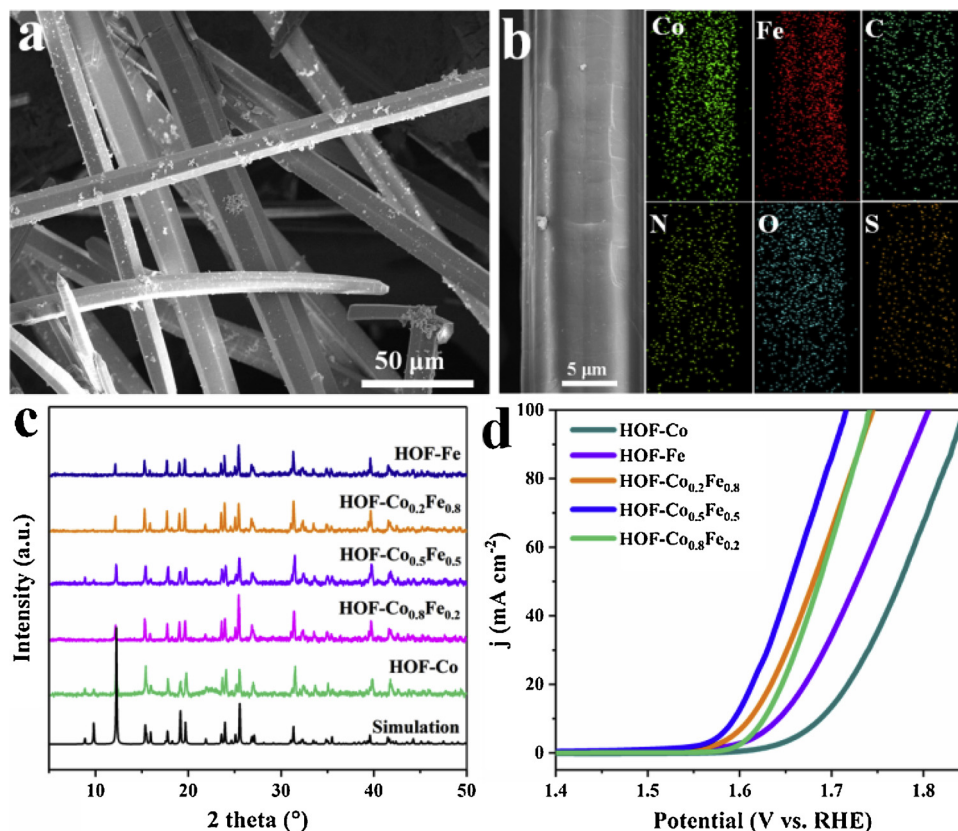


Fig. 2. a) SEM and b) SEM-EDS mapping images of HOF- $\text{Co}_{0.5}\text{Fe}_{0.5}$. c) PXRD patterns of different HOFs and simulated HOF-Co. d) Polarization curves of different samples tested in O_2 -saturated 1.0 M KOH.

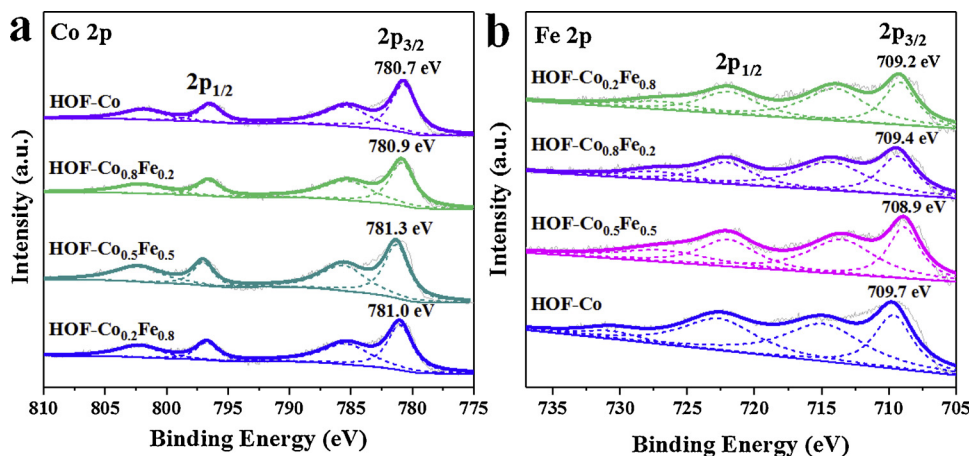


Fig. 3. XPS spectra in Co 2p region and b) the binding energy of Co 2p_{3/2} in different HOF samples.

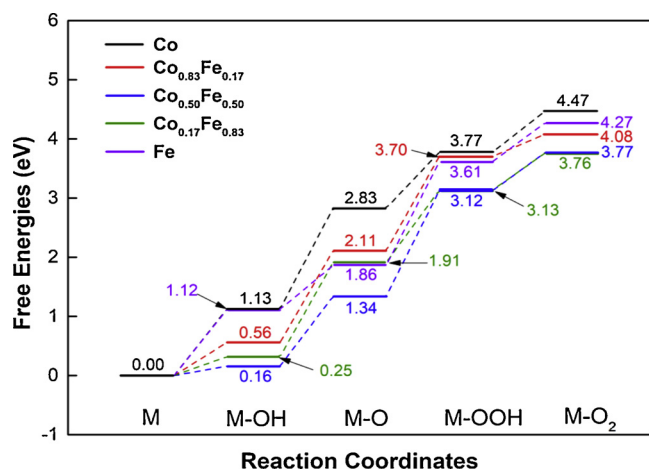


Fig. 4. Adsorption free energy for the OER pathway in HOF-Co, HOF-Co_{0.83}Fe_{0.17}, HOF-Co_{0.50}Fe_{0.50}, HOF-Co_{0.17}Fe_{0.83} and HOF-Fe.

and bimetallic synergetic effect.

It is well known that the potential application of electrocatalysts are often limited by the glassy carbon (GC) electrode [52]. By contrast, the nickel foam (NF) offers a promising alternative, which can promote electrolyte penetration, improve the conductivity and increase electrochemical active surface area [53]. Benefiting from the stepwise synthetic strategy, the HOFs materials in this work can be easily *in situ* grown on the NF. The success of anchoring HOF-Co_{0.5}Fe_{0.5} on NF is confirmed by SEM and PXRD (Fig. S9). As expected, the OER activity of HOF-Co_{0.5}Fe_{0.5} grown on NF (namely HOF-Co_{0.5}Fe_{0.5}/NF) can be largely enhanced with the overpotential down to 278 mV at 10 mA cm⁻² (Fig. S10a), smaller than the counterpart prepared by dropping method (namely HOF-Co_{0.5}Fe_{0.5}/NF-D, 307 mV). This remarkable value is also superior to the commercial IrO₂ benchmark and comparable to most of established top level metal-based electrocatalyst, MOF-derived electrocatalyst, and MOF electrocatalyst (Table S2). Furthermore, the Tafel slopes of HOF-Co_{0.5}Fe_{0.5}/NF, HOF-Co_{0.5}Fe_{0.5}/NF-D, HOF-Co_{0.5}Fe_{0.5}/GC, IrO₂/NF and NF were obtained by fitting the corresponding LSV curves (Fig. S10b) and then compared to reflect the OER kinetics of different samples. As expected, HOF-Co_{0.5}Fe_{0.5}/NF delivers the smallest Tafel slope of 59 mV dec⁻¹, which is much superior to IrO₂/NF (148 mV dec⁻¹), demonstrating the most fastest reaction kinetics in HOF-Co_{0.5}Fe_{0.5}/NF for OER process. To disclose the intrinsic OER activity, the TOF values of different electrodes were calculated to build a plot of TOF values against the applied overpotential (Fig. S11). It can be seen that the TOF value in HOF-Co_{0.5}Fe_{0.5}/NF is higher than those in HOF-Co_{0.5}Fe_{0.5}/NF-D and IrO₂/NF. To determine the amount of produced O₂

and Faradaic efficiency, a constant-potential test was carried out at the overpotential of 278 mV. The amount of O₂ measured using a Differential Air Pressure Gauge Manometer (CEM DT-8890) is well consistent with the theoretically calculated amount, exhibiting the Faradaic efficiency of as high as 99.9% (Fig. S12). The actual rate of O₂ evolution is about 2.09 mL/h. It should be pointed out that negligible activity was observed for pure NF. Correspondingly, the ECSA of HOF-Co_{0.5}Fe_{0.5}/NF is significantly enhanced by about 2.2 fold, in contrast to HOF-Co_{0.5}Fe_{0.5} dropped on GC (Fig. S13).

The stability of electrocatalyst during OER process is a key criterion to judge their practical application. Impressively, the negligible change of polarization curve before and after 1000 CV cycles and the current density after chronoamperometric test within 20 h at the constant overpotential of 278 mV is almost unchanged (Fig. S14). The PXRD pattern of HOF-Co_{0.5}Fe_{0.5}/NF after the chronoamperometric test of 20 h can still keep the characteristic diffractions as observed in the fresh HOF-Co_{0.5}Fe_{0.5}/NF samples (Fig. S15). SEM and TEM images also disclose that the HOF-Co_{0.5}Fe_{0.5}/NF sample after stability test can perfectly maintain the rod-like morphology (Fig. S16 and S17). The electronic states of HOF-Co_{0.5}Fe_{0.5}/NF before and after a 20 h durability test were also characterized by XPS measurement (Fig. S18). The slight increase of Co 2p_{3/2} binding energy after 20 h chronoamperometric test should be ascribed to the absorption of oxygen species or slight surface oxidation [54]. All these results strongly demonstrate the excellent stability and durability of HOF-Co_{0.5}Fe_{0.5}/NF for OER.

As discussed in the literature, for Co/Fe-based bimetallic electrocatalysts, Co species is generally regarded as the main active centres, and the incorporation of Fe can modulate the local electronic nature of Co species, thus improving the OER performance [55]. Thus, XPS characterizations were performed to understand the impact of Co-Fe electronic effect on OER activity. As shown in Fig. 3, the XPS spectrums of Co 2p and Fe 2p region in different HOFs have been deconvoluted and the bimetallic HOFs exhibit higher binding energy of Co 2p compared to monometallic HOF-Co while the binding energy of Fe 2p shifts to lower value in bimetallic HOFs, suggesting that incorporating Fe can indeed modulate the electronic structure of Co species and promote the electron transfer from Co to Fe [56,57]. Moreover, with the increase of Fe content, the binding energy of Co 2p spectrum increases firstly and then decreases, implying the optimal bimetallic effect at the Fe:Co ratio of 0.5:0.5.

To further understand the intrinsic OER activities of different samples, density functional theory (DFT) calculations were carried out. Both the monometallic HOFs (HOF-Co and HOF-Fe) and the bimetallic HOFs (HOF-Co_{0.83}Fe_{0.17}, HOF-Co_{0.50}Fe_{0.50}, and HOF-Co_{0.17}Fe_{0.83}) were comparatively studied. Fig. 4 shows the adsorption free energy for OH, O, OOH and O₂, which decides the OER activity [58]. It shows that the HOF-Co has the largest adsorption free energy for OH, O, OOH and O₂

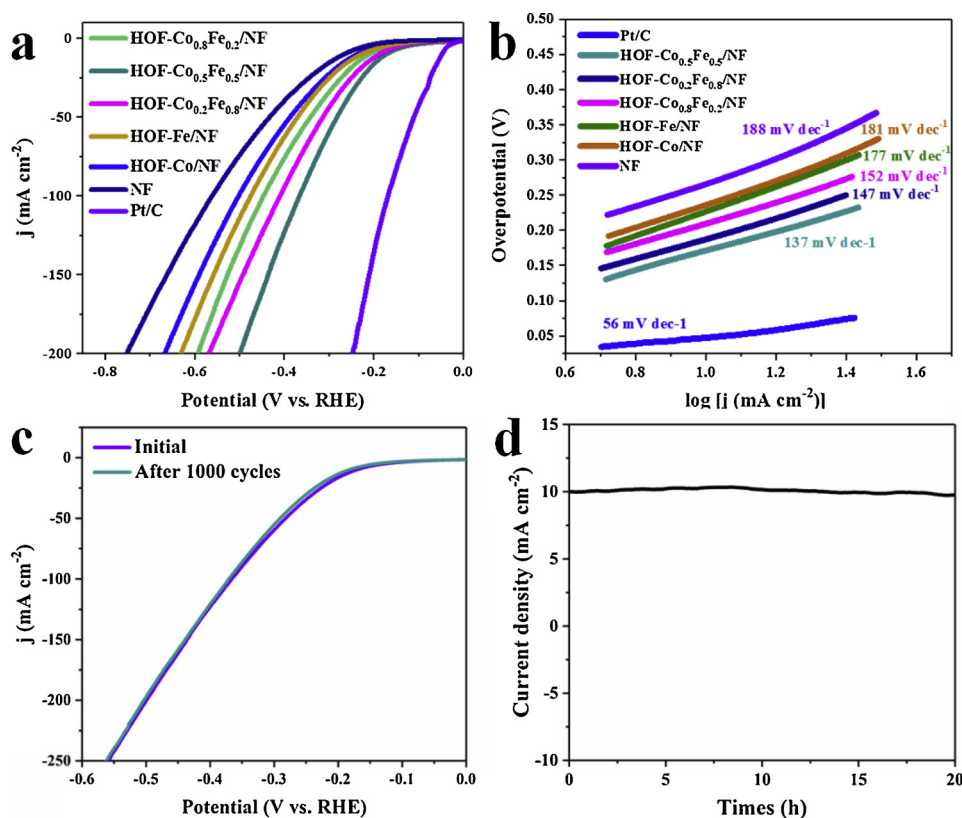


Fig. 5. a) Polarization curves and b) corresponding Tafel plots of different samples. c) Polarization curves of HOF-Co_{0.5}Fe_{0.5}/NF before and after 1000 cycles of CV scan. d) Chronoamperometric curve of HOF-Co_{0.5}Fe_{0.5}/NF at the overpotential of 170 mV.

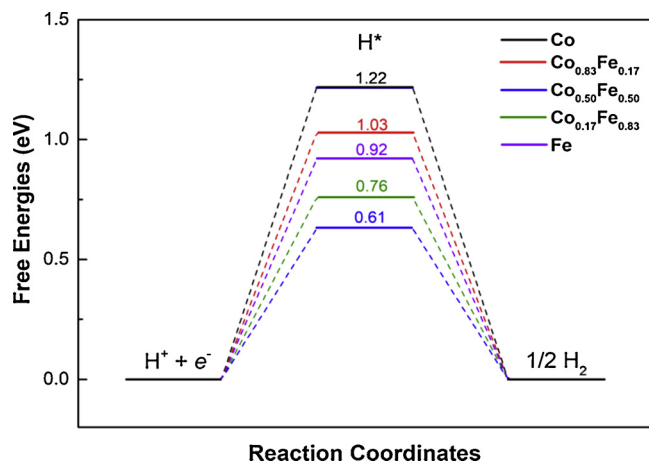


Fig. 6. Adsorption free energy of H adsorption on HOF-Co, HOF-Co_{0.83}Fe_{0.17}, HOF-Co_{0.50}Fe_{0.50}, HOF-Co_{0.17}Fe_{0.83} and HOF-Fe.

unanimously, whereas the HOF-Co_{0.5}Fe_{0.5} has the lowest adsorption free energy correspondingly, indicating that the HOF-Co_{0.5}Fe_{0.5} is the most active electrocatalyst for OER reactions, in well agreement with experimental observations.

Density of states (DOS) are further calculated to illuminate the electronic structure changes for these monometallic and bimetal HOFs as shown in Fig. S19. Specifically, the projected DOS for the *p* orbitals from O and the *d* orbitals from Co and Fe were listed. With the dopant of Fe, the vacant DOS above the Fermi level, which are mostly from the anti-bonding orbitals, shift down through the Fermi level. The DOS near the Fermi level increases significantly compared to that of the HOF-Co. As a result, it generally boosts the bimetal HOFs conductivity and their correlative electrocatalytic activity. In addition, the shifting down of

these anti-bonding orbitals weakens the O adsorption on the reactive metal (Co and Fe) sites according to the *d* band theory [59]. The weakening of O adsorption is conducive to the releasing of O₂; and it is critical for the OER activity enhancement.

The amount of doping is also essential for the OER activity. Although Co and Fe are both magnetic elements, the occupation of *d* orbitals is different, i.e. Co has three single occupied 3*d* orbitals whereas Fe has four single occupied 3*d* orbitals in their corresponding HOFs. The bonding of H₂O and metal center (Co/Fe), i.e. M–O (H₂O) bond mainly attribute to the interaction between the *p* orbitals of O and the *d* orbitals of the metals. As the occupation is different for Co and Fe, the energy level of the *d* bands is slightly different for Co and Fe, respectively. In case of doping, the DOS peak will be broadened due to the less overlap of the *d* bands of Co and Fe, and delocalized electrons around these Metal–O bonds. The delocalization of electrons will weaken the corresponding M–O(H₂O) bonds. As shown in Fig. S19, the DOS peak for HOF-Co_{0.5}Fe_{0.5} arising from the M–O(H₂O) bonding is the least sharp and the most wide among all the HOFs. The main reason is that the electron at the Metal–O bond for HOF-Co_{0.5}Fe_{0.5} is the most delocalized and leads to the weakest Metal–O bond. As a consequence, HOF-Co_{0.5}Fe_{0.5} becomes the most efficient electrocatalyst for OER reactions among all the bimetal HOFs.

Furthermore, we tested the HER activity of these HOF samples *in situ* grown on NF in 1.0 M KOH. Interestingly, these HOFs also render high HER activity, and HOF-Co_{0.5}Fe_{0.5}/NF shows the lowest overpotential of 170 mV at 10 mA cm^{−2}, relative to other HOFs (Fig. 5a), also giving the hierarchy of HOF-Co_{0.5}Fe_{0.5}/NF (170 mV) > HOF-Co_{0.2}Fe_{0.8}/NF (188 mV) > HOF-Co_{0.8}Fe_{0.2}/NF (211 mV) > HOF-Fe/NF (227 mV) > HOF-Co/NF (237 mV). Moreover, the plots of TOF values for HER catalysis against the applied overpotential in different electrodes demonstrate the most excellent intrinsic activity in HOF-Co_{0.5}Fe_{0.5}/NF compared to those of HOF-Co_{0.8}Fe_{0.2}/NF, HOF-Co_{0.2}Fe_{0.8}/NF, HOF-Fe/NF and HOF-Co/NF (Fig. S20). The

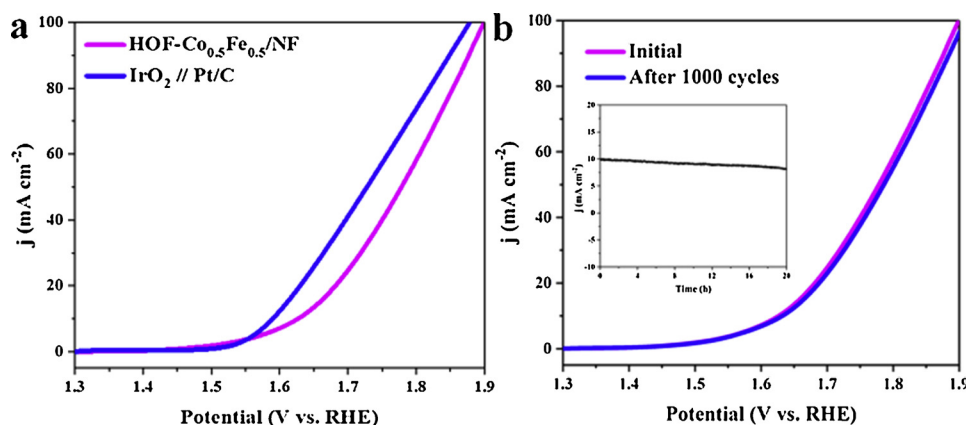


Fig. 7. a) The polarization curves for the overall water splitting and b) polarization curves for HOF-Co_{0.5}Fe_{0.5}/NF before and after 1000 cycles of CV scan with the inset for the chronoamperometric curve of HOF-Co_{0.5}Fe_{0.5}/NF at the voltage of 1.63 V.

corresponding Tafel slop calculated in HOF-Co_{0.5}Fe_{0.5}/NF is also smaller than the monometallic HOFs and other bimetallic HOFs (Fig. 5b), revealing more effective HER kinetics in HOF-Co_{0.5}Fe_{0.5}/NF. The results also imply that the optimal bimetallic effect is also beneficial for HER. A constant-potential test was performed at the overpotential of 170 mV to test the amount of generated H₂ and Faradaic efficiency. The generated H₂ is well in accordance with the theoretical value (Fig. S21). The actual rate of H₂ evolution is about 1.04 mL/h and the Faradaic efficiency reaches 99.9%. Further, the high stability of HOF-Co_{0.5}Fe_{0.5}/NF is confirmed by 1000 CV cycles and chronoamperometric test (Fig. 5c and d). The morphology and crystalline phase of HOF-Co_{0.5}Fe_{0.5}/NF after the chronoamperometric test were determined by SEM and PXRD characterizations. As shown in Fig. S22, the morphology remains nearly identical with that before. Moreover, the negligible change of crystalline phase was proved by PXRD pattern without any extra peaks (Fig. S23). The TEM images of HOF-Co_{0.5}Fe_{0.5}/NF shows no obvious change when compared with the pristine sample (Fig. S24). Subsequently, XPS measurement was carried out to examine the electronic state and chemical composition of Co species in HOF-Co_{0.5}Fe_{0.5}/NF. As revealed by Co 2p spectra (Fig. S25), the electronic state remained nearly unchanged compared to that in fresh HOF-Co_{0.5}Fe_{0.5}. These results undoubtedly prove the stability of HOF-Co_{0.5}Fe_{0.5}/NF during HER process.

To elucidate the origin of the best performance in HOF-Co_{0.5}Fe_{0.5}, the Gibbs free energy of hydrogen adsorption, which is closely associated with the HER performance, were performed for both the monometal and bimetal HOFs as shown in Fig. 6. The calculated adsorption free energy for HOF-Co_{0.5}Fe_{0.5} is indeed the lowest one at 0.61 eV, in line with the experimental observation. As mentioned above, the HOF-Co_{0.5}Fe_{0.5} has the most weak M–O(H₂O) bond due to the electron delocalization. The adsorption energy of H₂O is supposed to be less favorable for adsorption. To our surprise, the calculated adsorption energy for HOF-Co_{0.5}Fe_{0.5} is at -1.18 eV (Table S3). It is the most favorable one among all the monometal and bimetal HOFs. In consideration of the interaction for H₂O in HOFs mainly through the M–O and hydrogen bonding, thus since the M–O bonds are weakened and the adsorption energy increases, it can be logically deduced that the hydrogen bonding increases significantly. As the hydrogen bonds are formed between the O atoms from SO₄²⁻ and H atoms from the H₂O, it will ineluctably weaken the O–H bonds of H₂O. The stronger the hydrogen bonds are, the weaker the O–H bonds are. As a result, the HOF-Co_{0.5}Fe_{0.5} shows the best HER performance.

Based on the above OER and HER results, we next carried out the test of electrocatalytic water splitting in a two-electrode cell with HOF-Co_{0.5}Fe_{0.5}/NF as both the anode and the cathode. It is exciting to find that this material only requires the cell voltage of 1.63 V to reach 10 mA cm⁻² (Fig. 7a), which is comparable to the commercial metal-based Pt/

C//IrO₂ counterpart (1.59 V) and most reported outstanding electrocatalysts (Table S4). Moreover, the negligible change is found for polarization curve before and after 1000 CV scan, and it also exhibits high stability for overall water splitting within 20 h at the voltage of 1.63 V (Fig. 7b, insert). To the best of our knowledge, although there have developed a lot of crystal metal-organic compounds for OER and scarce case for HER; however, for the overall water splitting just by crystal metal-organic compound there is only one case in the literature [60,61]. Thus, our case should present the second.

4. Conclusions

In summary, we have demonstrated herein the possibility of using HOF as electrocatalyst for the overall water splitting. To circumvent the serious issues for traditional HOF materials such as bad stability in strong alkaline environment and extremely low electrocatalytic activity, we adopted a convenient and effective approach through constructing metal-complex based HOF. To finely tune the bimetallic effect, obtain highly crystalline bimetallic HOFs, and generate stable electrocatalyst, we further developed a step-by-step strategy to synthesize metal-complex based HOF, bimetallic HOFs, and NF-supported counterparts. The results show that the as-synthesized HOF-Co_{0.5}Fe_{0.5}/NF material enables outstanding electrocatalytic performance in both OER and HER, consequently leading to superior application in the overall water splitting. The DFT calculation shows that the synergistic effect from the strong hydrogen-bond interactions between coordinated water molecules and SO₄²⁻ ions and the bimetallic effect is responsible for such performance. Accordingly, these results open up an avenue to further design HOFs for electrocatalytic water splitting.

Declaration of Competing Interest

The authors declare that they have no known competing financial interests or personal relationships that could have appeared to influence the work reported in this paper.

Acknowledgements

We gratefully thank the financial support from the National Natural Science Foundation of China (21871047, 21661001), the Natural Science Foundation of Jiangxi Province of China (20181ACB20003), and the Senior Talent Research Start-up Fund of Shenzhen University (000263 and 000265).

Appendix A. Supplementary data

Supplementary material related to this article can be found, in the

online version, at doi:<https://doi.org/10.1016/j.apcatb.2019.117973>.

References

- [1] C. Tan, X. Cao, X.-J. Wu, Q. He, J. Yang, X. Zhang, J. Chen, W. Zhao, S. Han, G.-H. Nam, M. Sindoro, H. Zhang, *Chem. Rev.* 117 (2017) 6225–6331.
- [2] Z. Gao, F. Liu, L. Wang, F. Luo, *Appl. Surf. Sci.* 480 (2019) 548–556.
- [3] F.-S. Zhang, J. Wang, J. Luo, R. Liu, Z. Zhang, C. He, T. Lu, *Chem. Sci.* 9 (2018) 1375–1384.
- [4] Q. Hu, X. Liu, B. Zhu, L. Fan, X. Chai, Q. Zhang, J. Liu, C. He, Z. Lin, *Nano Energy* 50 (2018) 212–219.
- [5] E. Miner, T. Fukushima, D. Sheberla, L. Sun, Y. Surendranath, M. Dincă, *Nat. Commun.* 7 (2016) 10942–10948.
- [6] X. Zou, Y. Zhang, *Chem. Soc. Rev.* 44 (2015) 5148–5180.
- [7] P. Chen, K. Xu, T. Zhou, Y. Tong, J. Wu, H. Cheng, X. Lu, H. Ding, C. Wu, Y. Xie, *Angew. Chem. Int. Ed.* 55 (2016) 2488–2492.
- [8] T. Tang, W. Jiang, S. Niu, N. Liu, H. Luo, Y. Chen, S. Jin, F. Gao, L. Wan, J. Hu, J. Am. Chem. Soc. 139 (2017) 8320–8328.
- [9] Q. Hu, G. Li, X. Liu, B. Zhu, X. Chai, Q. Zhang, J. Liu, C. He, *Angew. Chem. Int. Ed.* 58 (2019) 4318–4322.
- [10] Z. Gao, F.-Q. Liu, L. Wang, F. Luo, *Inorg. Chem.* 58 (2019) 3247–3255.
- [11] F. Sun, G. Wang, Y. Ding, C. Wang, B. Yuan, Y. Lin, *Adv. Energy. Mater.* 18 (2018) 1800584–1800594.
- [12] Y. Zheng, Y. Jiao, Y. Zhu, Q. Cai, A. Vasileff, L. Li, Y. Han, Y. Chen, S. Qiao, J. Am. Chem. Soc. 139 (2017) 3336–3339.
- [13] J. Li, Y. Wang, C. Liu, S. Li, Y. Wang, L. Dong, Z. Dai, Y. Li, Y. Lan, *Nat. Commun.* 7 (2016) 11204–11211.
- [14] J. Shen, P. Liao, D. Zhou, C. He, J. Wu, W. Zhang, J. Zhang, X. Chen, J. Am. Chem. Soc. 139 (2017) 1778–1781.
- [15] X. Zhang, F. Zhou, W. Pan, Y. Liang, R. Wang, *Adv. Funct. Mater.* 28 (2018) 1804600–1804607.
- [16] X. Wang, L. Dong, M. Qiao, Y. Tang, J. Liu, Y. Li, S. Li, J. Su, Y. Lan, *Angew. Chem. Int. Ed.* 57 (2018) 9660–9664.
- [17] F. Zhang, J. Wang, J. Luo, R. Liu, Z. Zhang, C. He, T. Lu, *Chem. Sci.* 9 (2018) 1375–1384.
- [18] X. Lu, P. Liao, J. Wang, J. Wu, X. Chen, C. He, J. Zhang, G. Li, X. Chen, J. Am. Chem. Soc. 138 (2016) 8336–8339.
- [19] F. Song, K. Schenk, X. Hu, *Energy Environ. Sci.* 9 (2016) 473–477.
- [20] Y. Xu, Z. Ye, J. Ye, L. Cao, R. Huang, J. Wu, D. Zhou, X. Zhang, C. He, J. Zhang, X. Chen, *Angew. Chem. Int. Ed.* 131 (2019) 145–1149.
- [21] J. Li, W. Huang, M. Wang, S. Xi, J. Meng, K. Zhao, J. Jin, W. Xu, Z. Wang, X. Liu, Q. Chen, L. Xu, X. Liao, Y. Jiang, K. Owusu, B. Jiang, C. Chen, D. Fan, L. Zhou, L. Mai, *ACS Energy Lett.* 4 (2019) 285–292.
- [22] C. Cao, D. Ma, Q. Xu, X. Wu, Q. Zhu, *Adv. Funct. Mater.* 29 (2019) 1807418–1807425.
- [23] W. Cheng, Zhao X, H. Su, F. Tang, W. Che, H. Zhang, Q. Liu, *Nat. Energy.* 4 (2019) 115–122.
- [24] W. Zhou, D. Huang, Y. Wu, J. Zhao, T. Wu, J. Zhang, D. Li, C. Sun, P. Feng, X. Bu, *Angew. Chem. Int. Ed.* 58 (2019) 4227–4231.
- [25] C. Tang, N. Cheng, Z. Pu, W. Xing, X. Sun, *Angew. Chem. Int. Ed.* 54 (2015) 9351–9355.
- [26] Y.-Q. Zhang, B. Ouyang, J. Xu, G.-C. Jia, S. Chen, R.S. Rawat, H.J. Fan, *Angew. Chem. Int. Ed.* 55 (2016) 8670–8674.
- [27] N. Jiang, B. You, M. Sheng, Y. Sun, *Angew. Chem. Int. Ed.* 54 (2015) 6349–6352.
- [28] C.X. Guo, Y. Zheng, J. Ran, F. Xie, M. Jaroniec, S. Qiao, *Angew. Chem. Int. Ed.* 56 (2017) 8539–8543.
- [29] Q. Hu, G. Li, G. Li, X. Liu, B. Zhu, X. Chai, Q. Zhang, J. Liu, C. He, *Adv. Energy Mater.* 9 (2019) 1803867.
- [30] X. Cui, P. Ren, D. Deng, J. Deng, X. Bao, *Energy Environ. Sci.* 9 (2016) 123–129.
- [31] Z. Chen, H. Xu, Y. Ha, X. Li, M. Liu, R. Wu, *Appl. Catal. B: Environ.* 250 (2019) 213–223.
- [32] A. Chaix, G. Mouchaham, A. Shkurenko, P. Hoang, B. Moosa, P. Bhatt, K. Adil, K. Salama, M. Eddaoudi, N. Khashab, J. Am. Chem. Soc. 140 (2018) 14571–14575.
- [33] J. Lü, C. PereKrap, M. Suyetin, N. Alsmail, Y. Yan, S. Yang, W. Lewis, E. Bichoutskaia, C. Tang, A. Blake, R. Cao, M. Schröer, J. Am. Chem. Soc. 136 (2014) 12828–12831.
- [34] R. Kubota, S. Tashiro, M. Shiro, M. Shionoya, *Nat. Chem.* 6 (2014) 913–918.
- [35] J. Lü, R. Cao, *Angew. Chem. Int. Ed.* 55 (2016) 9474–9480.
- [36] Y. Luo, X. He, D. Hong, C. Chen, F. Chen, J. Jiao, L. Zhai, L. Guo, B. Sun, *Adv. Funct. Mater.* 28 (2018) 1804822–1804828.
- [37] R.-B. Lin, Y.-B. He, P. Li, H.-L. Wang, W. Zhou, B.-L. Chen, *Chem. Soc. Rev.* 48 (2019) 1362–1389.
- [38] I. Hisaki, Y. Suzuki, E. Gomez, Q. Ji, N. Tohna, T. Nakamura, A. Douhal, J. Am. Chem. Soc. 141 (2019) 2111–2121.
- [39] G. Xing, I. Bassanetti, S. Bracco, M. Negroni, C. Bezuidenhout, T. Ben, P. Sozzani, A. Comotti, *Chem. Sci.* 10 (2019) 730–736.
- [40] J. Perego, D. Piga, S. Bracco, P. Sozzani, A. Comotti, *Chem. Commun.* 54 (2018) 9321–9324.
- [41] Y. Li, M. Handke, Y. Chen, A. Shtukenberg, C. Hu, M. Ward, J. Am. Chem. Soc. 140 (2018) 12915–12921.
- [42] I. Hisaki, Y. Suzuki, E. Gomez, B. Cohen, N. Tohna, A. Douhal, *Angew. Chem. Int. Ed.* 57 (2018) 12650–12655.
- [43] Z. Bao, D. Xie, G. Chang, H. Wu, L. Li, W. Zhou, H. Wang, Z. Zhang, H. Xing, Q. Yang, M. Zaworotko, Q. Ren, B. Chen, J. Am. Chem. Soc. 140 (2018) 4596–4603.
- [44] X. Luo, X. Jia, J. Deng, J. Zhong, H. Liu, K. Wang, D. Zhong, J. Am. Chem. Soc. 135 (2013) 11684–11687.
- [45] J. Mahmood, S. Kim, H. Noh, S. Jung, I. Ahmad, F. Li, J. Seo, J. Baek, *Angew. Chem. Int. Ed.* 57 (2018) 3415–3420.
- [46] W. Yang, A. Greenaway, X. Lin, R. Matsuda, A. Blake, C. Wilson, W. Lewis, P. Hubbert, S. Kitagawa, N. Champness, M. Schröer, J. Am. Chem. Soc. 132 (2010) 14457–14469.
- [47] P. Sozzani, S. Bracco, A. Comotti, L. Ferretti, R. Simonutti, *Angew. Chem. Int. Ed.* 117 (2005) 1850–1854.
- [48] H. Wang, B. Li, H. Wu, T. Hu, Z. Yao, W. Zhou, S. Xiang, B. Chen, J. Am. Chem. Soc. 137 (2015) 9963–9970.
- [49] G. Kresse, J. Furthmüller, *Phys. Rev. B* 54 (1996) 11169.
- [50] J.P. Perdew, K. Burke, M. Ernzerhof, *Phys. Rev. Lett.* 77 (1996) 3865.
- [51] J.K. Nørskov, J. Rossmeisl, A. Logadottir, L. Lindqvist, J.R. Kitchin, T. Bligaard, H. Jonsson, *J. Phys. Chem. B* 108 (2004) 17886.
- [52] F. Li, Q. Shao, X. Huang, J. Lang, *Angew. Chem. Int. Ed.* 57 (2018) 1906–1910.
- [53] M. Qian, S. Cui, D. Jiang, L. Zhang, P. Du, *Adv. Mater.* 29 (2017) 1704075–1704080.
- [54] J. Li, W. Huang, M. Wang, S. Xi, J. Meng, K. Zhao, J. Jin, W. Xu, Z. Wang, X. Liu, Q. Chen, L. Xu, X. Liao, Y. Jiang, K.A. Owusu, B. Jiang, C. Chen, D. Fan, L. Zhou, L. Mai, *ACS Energy Lett.* 4 (2019) 285–292.
- [55] B. Zhang, H. Wang, Z. Zuo, H. Wang, J. Zhang, *J. Mater. Chem. A* 6 (2018) 15728–15737.
- [56] H. Zhang, Z. Ma, J. Duan, H. Liu, G. Liu, T. Wang, K. Chang, M. Li, L. Shi, X. Meng, K. Wu, J. Ye, *ACS Nano* 10 (2016) 684–694.
- [57] Y. Zhang, W. Li, L. Lu, W. Song, C. Wang, L. Zhou, J. Liu, Y. Chen, H. Jin, Y. Zhang, *Electrochim. Acta* 265 (2018) 497–506.
- [58] J. Nørskov, J. Rossmeisl, A. Logadottir, L. Lindqvist, J. Kitchin, T. Bligaard, H. Jonsson, *J. Phys. Chem. B* 108 (2004) 17886–17892.
- [59] B. Hammer, J. Nørskov, *Adv. Catal.* 45 (2000) 71–129.
- [60] X. Zhao, P. Pachfule, S. Li, J. Simke, J. Schmidt, A. Thomas, *Angew. Chem. Int. Ed.* 130 (2018) 9059–9064.
- [61] J. Duan, S. Chen, C. Zhao, *Nat. Commun.* 8 (2017) 15341.